Nanomechanical Properties and Failure Mechanisms of Two-Dimensional Metal-Organic Framework Nanosheets

Zhixin Zeng[1], *Irina S. Flyagina*[1,2] and *Jin-Chong Tan*[1,*]

[1]Multifunctional Materials & Composites (MMC) Laboratory, Department of Engineering Science, University of Oxford, Parks Road, Oxford, OX1 3PJ, United Kingdom.

[2]A.N. Frumkin Institute of Physical Chemistry and Electrochemistry of the Russian Academy of Sciences, 31 Leninsky prospect, Moscow, 119071, Russia.

*E-mail: jin-chong.tan@eng.ox.ac.uk

KEYWORDS: *nanoindentation, atomic force microscopy (AFM), metal-organic nanosheet (MON), nanoscale mechanical properties, strain rate, interfacial sliding, fracture, delamination, finite-element model (FEM)*

ABSTRACT

Nanoscale mechanical properties measurement of porous nanosheets presents many challenges. Herein we show atomic force microscope (AFM) nanoindentation to probe the nanoscale mechanical properties of a 2-D metal-organic framework (MOF) nanosheet material, termed CuBDC [copper 1,4-benzenedicarboxylate]. The sample thickness was ranging from ~10 nm (tens of monolayers) up to ~400 nm (stack of multilayers). In terms of its elastic-plastic properties, the Young's modulus (E ~ 22.9 GPa) and yield strength (σ_Y ~ 448 MPa) have been determined in the through-thickness direction. Moreover, we have characterized the failure mechanisms of the CuBDC nanosheets, where three failure mechanisms have been identified: interfacial sliding, fracture of framework, and delamination of multilayered nanosheets. Threshold forces and corresponding indentation depths corresponding to the failure modes have been determined. To gain insights into the failure mechanisms, we employ finite-element models with cohesive elements to simulate the interfacial debonding of a stack of 2-D nanosheets during the indentation process. The nanomechanical AFM methodology elucidated here will be pertinent to the study of other 2-D hybrid nanosheets and *van der Waals* solids.

I. BACKGROUND

Because the underlying structure of crystalline nanomaterials controls their functions, understanding the fundamental structure-property relations is important to enable practical applications of new materials.[1-4] Amongst two-dimensional (2-D) nanomaterials, we will focus on metal-organic framework (MOF) nanosheets which show benefits in several potential applications. For example, novel devices constructed from 2-D nanosheets show good tunability and efficacy in capacitance,[5,6] energy conversion,[7] electrocatalysis,[8] luminescence,[9] and gas separation.[10] While there are predictions of certain mechanical properties of 2-D structures at nanoscale using theoretical techniques such as density functional theory[11,12] and molecular dynamics,[13-16] hitherto, there is no rigorous experimental studies for quantifying the nanoscale mechanical properties of porous MOF nanosheets encompassing the elastic-plastic regime. Lack of systematically characterized experimental data of mechanical behavior is one of the factors that hinders confident evaluation of the practicability of MOF nanosheets. The mechanical property characterization of nanosheets *via* an experimental approach is complicated owing to the mutual interplay between the adjacent nanosheets (*viz.* interlayer interactions),[17] not to mention other major obstacles, such as the difficulties with small sample preparation, precise implementation of the fine-scale measuring techniques, and accurate interpretation of structural failure data.

A number of mechanical characterization experiments on nanosheets have been reported to date, where the depth-sensing indentation techniques have been employed.[18-21] This includes the use of atomic force microscope (AFM)-based nanoindentation and the instrumented nanoindentation techniques.[22] Thus far, studies have concentrated on either the ultra-stiff nanosheets, in particular graphene (Young's modulus, E ~1 TPa)[20,23-25] and boron nitride (E ~250 GPa),[17,26] or the very soft biological samples such as protein nanosheets.[27] Although there are a few experiments performed on nanosheets with stiffness in the range of a few gigapascals to tens of gigapascals, such as the dense 2-D hybrid framework of Mn 2,2-dimethylsuccinate nanosheets (E = 9.4 – 20.9 GPa depending on crystal orientation due to anisotropy)[28] and the bismuth telluride nanosheets (E = 11.7 – 25.7 GPa),[29] very few studies have systematically explored the mechanical behavior of porous MOF nanosheets. There is a report on the AFM nanoindentation of large flakes of $[Cu(\mu\text{-}pym_2S_2)(\mu\text{-}Cl)]_n$ MOF nanosheets, where the 2-D samples were suspended over a holey SiO_2 substrate and probed by an AFM tip in bending mode to estimate its Young's modulus and rupture stress.[30]

In this work, we demonstrate a direct AFM-based nanoindentation approach (unlike the foregoing AFM bending method)[20,30] to achieve quantitative study of the nanoscale mechanics of porous 2-D MOF nanosheets. Using a combination of indentation measurements and finite-element modeling, we have determined not only the elastic-plastic properties, but also gained a deeper understanding of the specific deformation mechanisms responsible for structural failures of 2-D nanosheets. It is envisaged that the methodology and analysis exemplified in this study will be applicable to characterize a vast range of topical 2-D *van der Waals* materials.[31]

II. Characterization of 2-D CuBDC Metal-Organic Nanosheets

The copper 1,4-benzenedicarboxylate (CuBDC) nanosheets, an example of MOF nanosheets, has been selected as the model material to develop the AFM nanoindentation technique for quantifying the nanoscale mechanical properties of 2-D MOF structures. CuBDC is composed of the square-planar copper(II) dimers coordinated to the BDC linkers.[32] CuBDC crystallizes in the monoclinic *C*2/*m* space group, where its adjacent nanosheets form a porous layered architecture as depicted Figure 1.

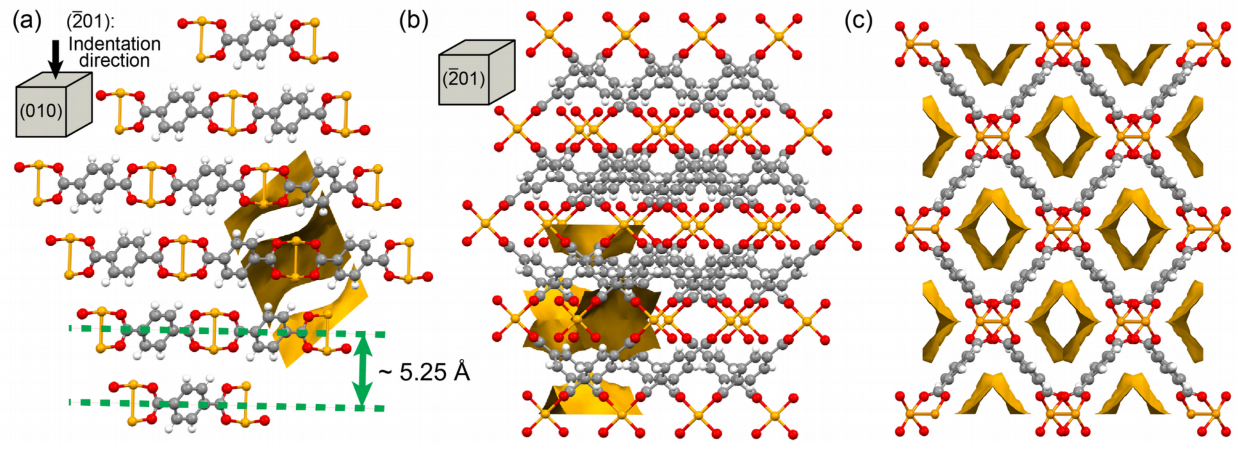

Figure 1. 2-D crystalline structure of the CuBDC layered framework. The dinuclear copper atoms are coordinated to the BDC linkers to form the copper paddle wheels. Pore channels are designated as yellow surfaces, corresponding to the solvent accessible volume using a probe size of 1.2 Å. (a) View down the [010] crystal axis, showing the stacking direction of the 2-D layers, in which the AFM nanoindenter penetrates along the $[\bar{2}01]$ crystal axis (i.e. downward arrow). (b) View down the $[\bar{2}01]$ axis. (c) View down the pore channels oriented along the [001] crystal axis. Oxygen, hydrogen and carbon atoms are shown in red, white, and grey, respectively.

The CuBDC nanosheets form thin 2-D crystals with a rectangular morphology as shown in Figure 2. The constituent CuBDC layers are stacked along the $[\bar{2}01]$ crystal axis and held by *van der Waals* forces, yielding a periodic framework structure (Figure 1a). From the AFM topographic images, it can be seen that the thickness of the CuBDC nanosheets ranges from ~10 nm (*viz.* the thinnest nanosheet consists of ~19 monolayers as shown in Figure 2c) to 400 nm (comprising hundreds of monolayers). Exfoliation of thin nanosheets out of the thicker multilayered stacks is important since these thin nanosheets offer a source of building blocks for constructing 2-D thin-film devices and flexible electronics.[7,33] Moreover, it has been reported that a composite mixed-matrix membrane made from exfoliated CuBDC embedded in a polymer matrix has excellent separation performance in a gas mixture of CO_2 and CH_4.[10]

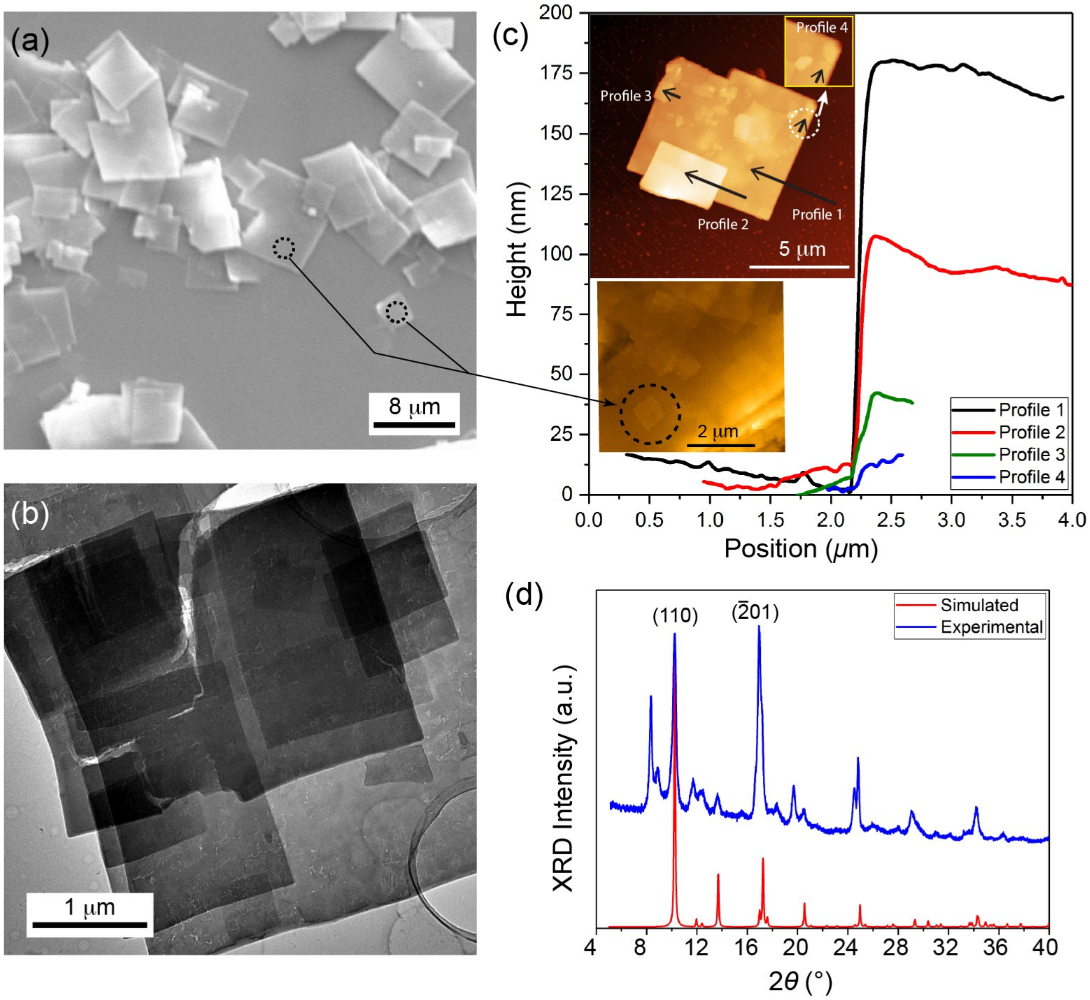

Figure 2. Characterization of the CuBDC nanosheets. (a) Scanning electron microscope (SEM) image; (b) Transmission electron microscope (TEM) image; (c) Atomic force microscope (AFM) images of the multilayered CuBDC nanosheets. (d) Experimental and simulated X-ray diffraction (XRD) patterns. Note that the two extra peaks at $2\theta \sim 8.3°$ and $\sim 8.9°$ are due to thermal desolvation of the framework reversible with addition of solvent molecules.[34]

Because the multilayered CuBDC nanosheets are held together by weak *van der Waals* forces, there is risk of delamination and other forms of interfacial failure caused by the sliding of nanosheets in shear deformation. Therefore, design and fabrication of functional devices integrating nanosheets will require an improved understanding of not only the common mechanical properties such as the elastic moduli, but also knowledge of interfacial failure modes since the sliding and rupture of nanosheets could affect function of the device. Furthermore, the interfacial failure between the nanosheets will impede accurate measurement by depth-sensing indentation technique, resulting in distortion of the indenter load-penetration depth (P-h) data or erroneous indenter-to-sample contact area. In this study, we address these challenges to enable quantitative determination of intrinsic 2-D mechanical behaviors.

III. RESULTS AND DISCUSSION

A. Quantification of Through-Thickness Elasticity

Figure 3a shows the representative load-displacement (P-h) curves obtained from AFM nanoindentation measurements, for a series of experiments where the maximum surface penetration depth was varied from about 10 nm to 32 nm. Figure 3b presents the Young's modulus (E) values of the nanosheets derived from a total of 56 nanoindentation experiments. It can be seen that the through-thickness stiffness of the CuBDC nanosheets measured by a low unloading strain rate is highly scattered and overestimated (up to E ~52 GPa). This is likely due to time-dependent deformations, such as creep deformation that will exaggerate the stiffness. Therefore an augmented unloading strain rate method[22] was implemented (see Methods), with which we found the Young's modulus starts to converge with an increasing unloading strain rate.

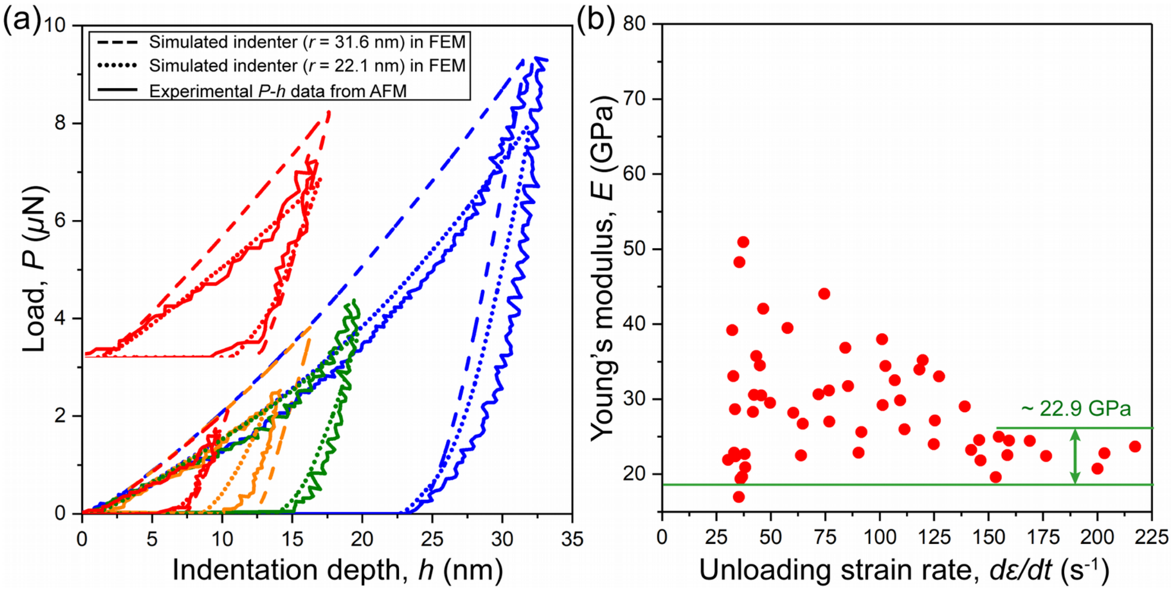

Figure 3. (a) Representative indentation load versus surface penetration depth (*P*-*h*) curves measured by AFM nanoindentation experiments (solid lines) and modeled by finite-element method (FEM, dashed and dotted lines for indentation using the two simulated indenter tips with a tip radius of 31.6 nm and 22.1 nm, respectively). Both the elastic and plastic deformation behaviors predicted by the FEM models are resembling the experimental data. (b) Young's modulus (*E*) of the CuBDC nanosheets determined using the Oliver & Pharr method, plotted as a function of the unloading strain rate of the nanoindenter tip.

When the unloading strain rate surpasses ~140 s^{-1}, the through-thickness stiffness value was found to be converged to an arithmetic mean of E ~ 22.9 GPa (Figure 3b). The Poisson's ratio of CuBDC was taken as $\nu = 0.4$; its effect on the Young's modulus of the CuBDC nanosheet is given in the Supporting Information (see Figure S11). The dashed and dotted curves in Figure 3a are the resulting P-h curves predicted by the FE model by assuming an ideal material (without material failure). The material properties defined in the model matches the elastic constants (E, ν) determined from the AFM nanoindentation experiments and the plasticity obtained from the iterative method (see section below).

B. Quantification of Plastic Deformation and Pile-up: Analysis using an Iterative Method

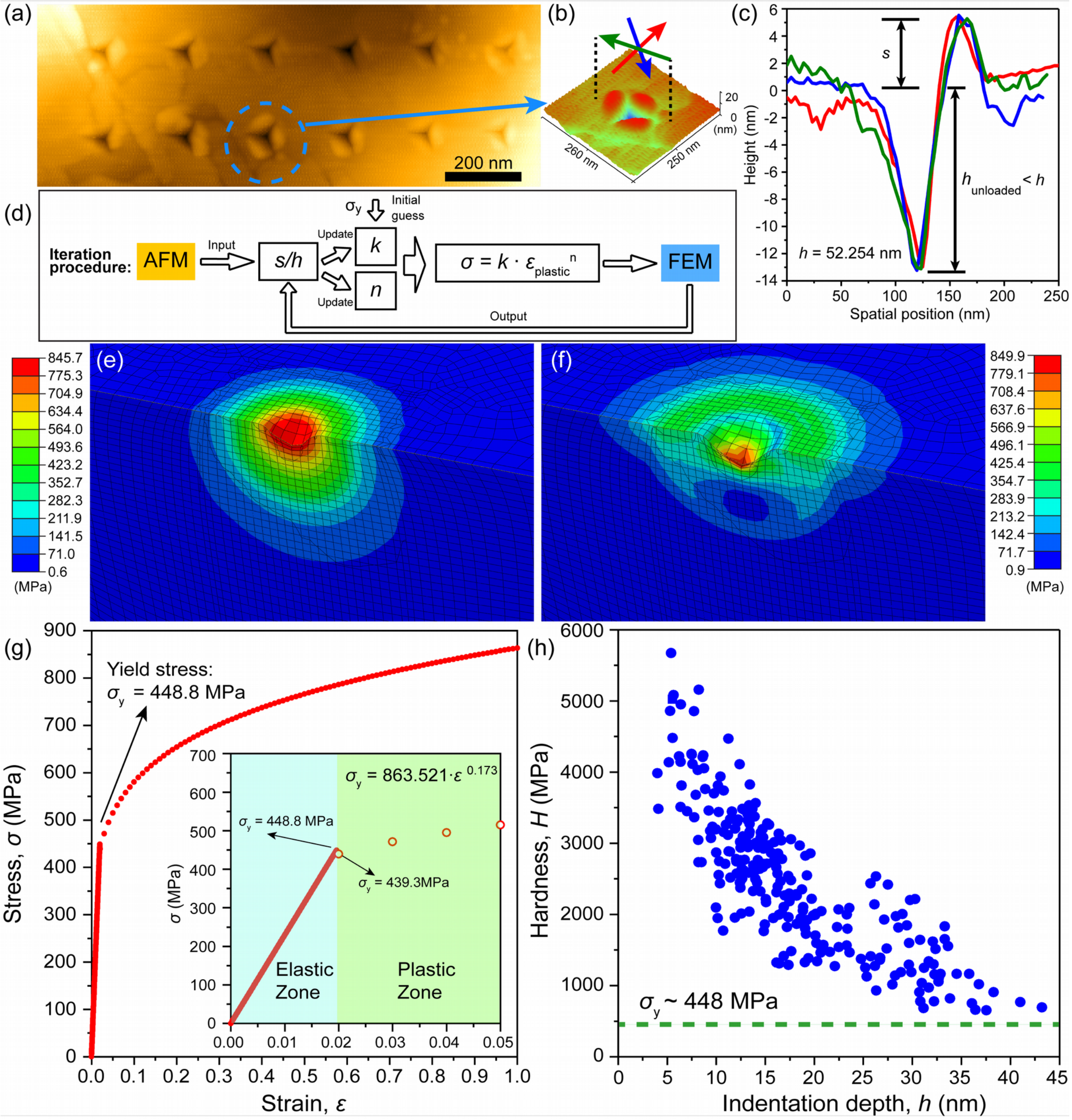

Figure 4. (a) AFM height images of residual indents on a stack of CuBDC nanosheets, where the pile-ups generated by the cube-corner indenter are clearly visible. (b) Height profiles shown as a 3-D depth color map, where the sectional profiles marked by the three arrows are plotted in (c). (d) Procedure of the iterative method. (e,f) Finite-element model showing the Mises stress contour of the simulated indentation employing a contact-area equivalent conical tip (details in

Table S1): (e) indentation at the state of the loading stage, and (f) the model at the fully unloaded stage (the indenter is not shown for clarity). (g) Stress-strain curve showing the elastic-plastic transition behavior of the CuBDC nanosheet around the yield point σ_y. (h) Hardness plotted as a function of the indentation depth; the value of the yield stress of the CuBDC nanosheets is approximated by the dashed line.

Plastic deformation is an important factor to be considered in indentation experiments and it is associated with the height of the residual indentation pile-up (Figure 4a-c). Systematic discussion about the analysis of indentation pile-ups of (monolithic) elastic-plastic solids has been done by Taljat and Pharr.[35] In this study, we employed finite-element (FE) modeling (Figure 4e-f) in combination with an iterative method (Figure 4d) to establish the plastic deformation behavior of the nanosheets, on the basis of the correlation between the plasticity and the height of the pile-ups formed in the periphery of the indents. The flow chart in Figure 4d summarizes the procedures of the iterative method, in which the results obtained from both the AFM-based nanoindentation experiments and the FE model were utilized to derive the value of the yield stress (see Methods).

As shown in Figure 4g, we found the yield stress of the CuBDC nanosheets lie in the range of $\sigma_y = 439 – 449$ MPa, bridging the elastic and plastic zones. Herein we propose that the yield phenomenon is linked to the plastic flow of the 2-D layered architecture prevalent in the CuBDC nanosheets, as evidenced by the large pile-ups observed in the vicinity of the residual indents, see Figures 4b-c. Hardness results from AFM nanoindentation is shown in Figure 4h. Nonetheless, hardness of a layered 2-D structure is significantly influenced by the sliding movement of the interlayers (*viz.* the sliding tendency),[17] where the indentation depth can no longer indicate the true resistance of the nanosheets against plastic deformation.

C. Identification of Failure Mechanisms

- **Nanoscale 2-D failures causing distortions of the indentation curves**

AFM nanoindentation was employed to characterize the mechanical failures of the CuBDC nanosheets, our aim is to understand the origin and characteristics of the different failure modes. Figure 5 shows the distortions of the *P*-*h* curves because of nanosheet failures from indentation. We propose three distinctive deformation modes underpinning the failure of the CuBDC nanosheets: Mode I – slippage between nanosheets, Mode II – fracture of nanosheets, and Mode III – delamination of nanosheets.

In Mode I, the coplanar nanosheets are separated by the penetrating indenter causing the nanosheets to slide sideways under shear deformation. Layer separation occurs since the coplanar nanosheets were weakly bound by *van der Waals* interactions. Typically, sliding of the nanosheets produces the stepwise distortion in the measured *P*-*h* curves, which is resembling the "pop-in" phenomenon observed in other 2-D materials.[28] During the slippage failure, a force analysis has been conducted (Figure 6a) to shed light on the underlying mechanism. In Mode II – the fracture of CuBDC framework was due to stress concentration generated by the indenter, and the phenomenon can be detected as the "humps" observed in the *P*-*h* curves. A similar failure mode has been reported in the two-layer stacked graphene indented by AFM[23] and the boron nitride nanosheets studied by *in situ* indentation.[36] For Mode III – during the loading stage, bending of a stack of nanosheets can lead to interlayer delamination failure, ascribed to the bending moment from the peripheral regions of the indent. In other words, as illustrated in Figure 6b, the stretching of the cohesive layer normal to the nanosheet plane eventually causes breakage of the adjacent nanosheets. In addition, the "pop-out" and recovery phenomena at the unloading stage have been observed and their mechanisms will be discussed below.

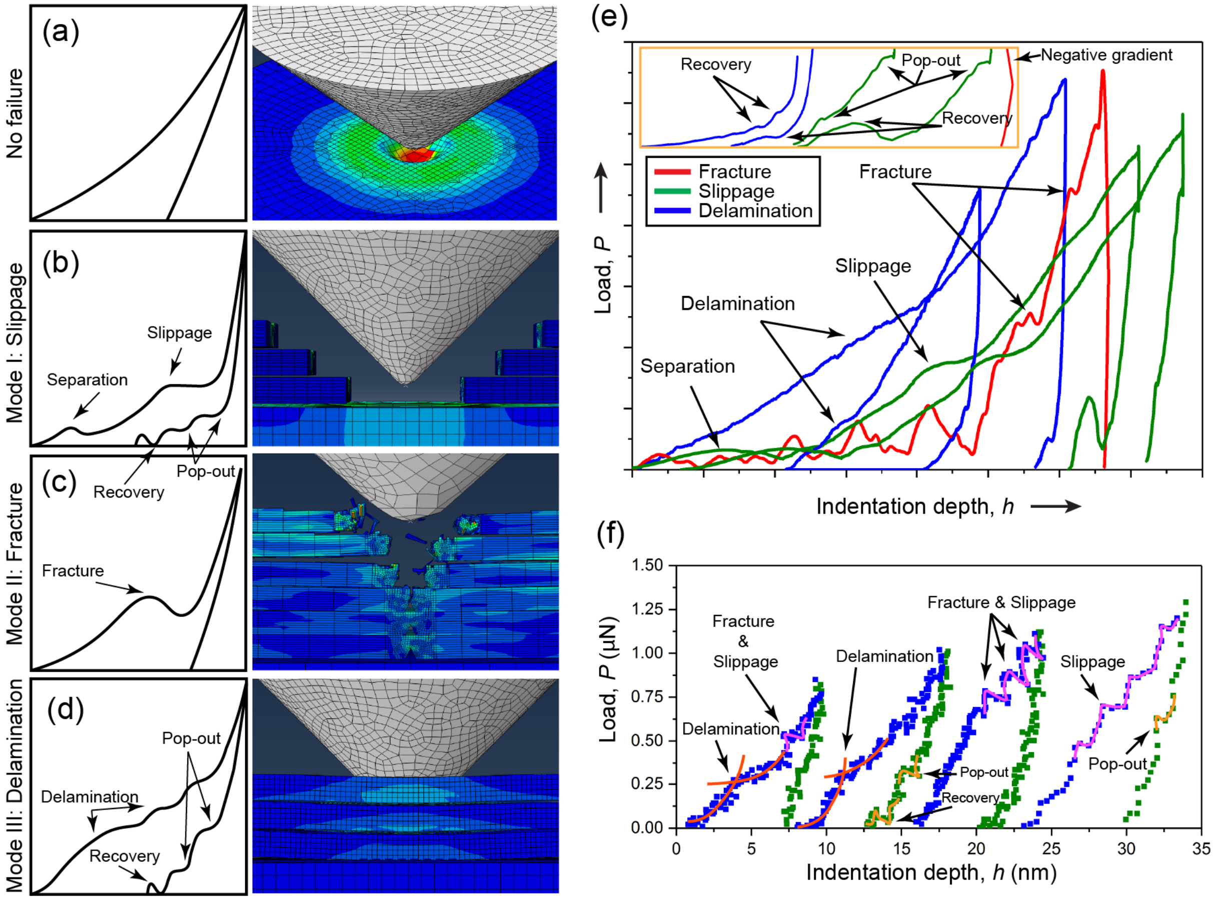

Figure 5. (a-d) Schematics illustrating the possible distortions of the *P*-*h* curves due to different nanosheet failure modes, the corresponding FE models are shown on the right panels. For comparison, (a) depicts the AFM nanoindentation of an ideal nanosheet stack (*viz.* perfectly bonded multilayers) without any material failure. (e) The FE models capture the main characteristics observed in the experimental *P*-*h* curves in (f) measured by AFM nanoindentation. The inset in (e) shows the magnified view of the unloading curves from FE modeling.

- **Force analysis to understand threshold forces of specific failures modes**

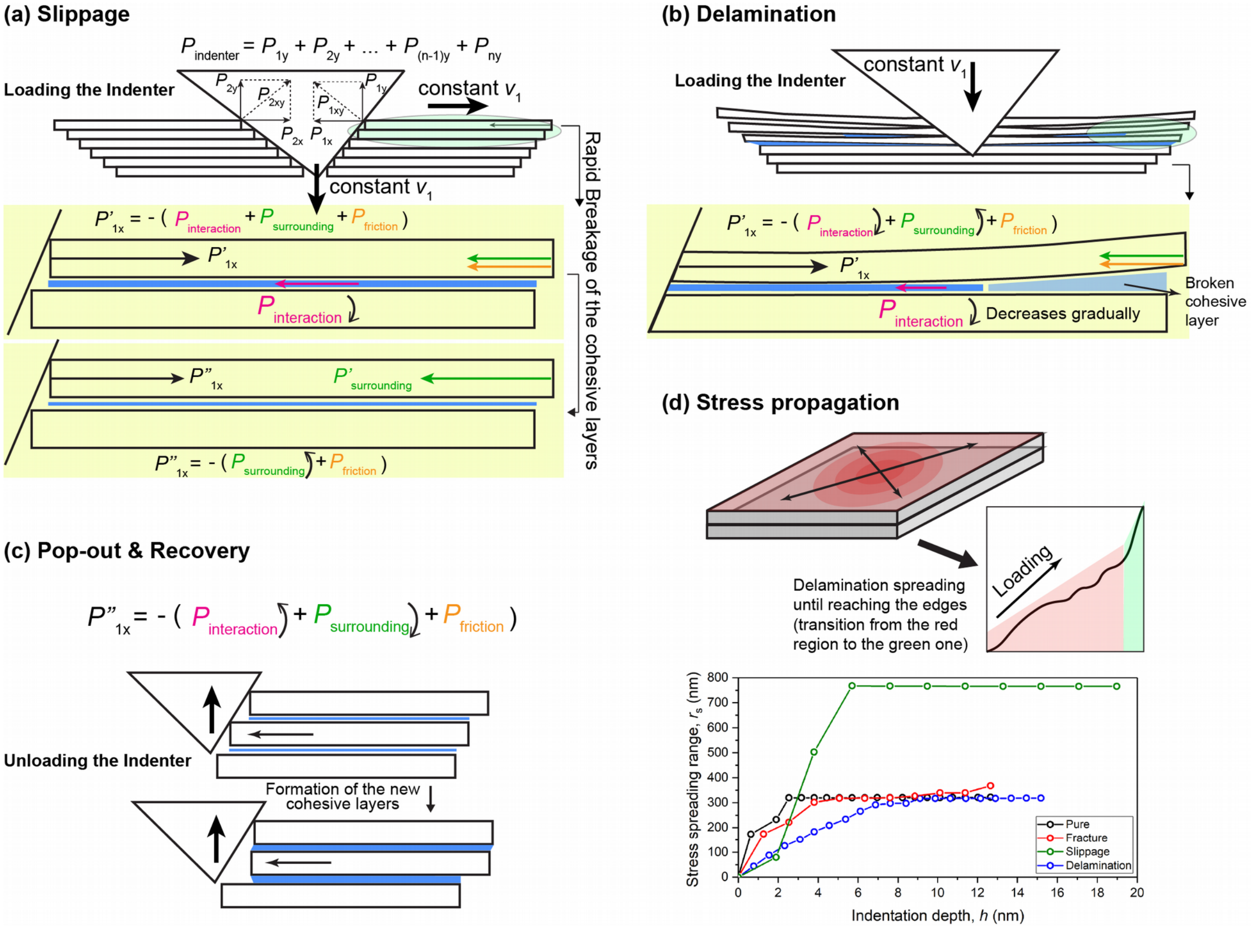

Figure 6. Schematic illustration of the evolution of the resolved forces between the indenter and a stack of nanosheets as well as between adjacent nanosheets under different failure modes: (a) interfacial slippage at loading due to shear, (b) delamination at loading due to bending, and (c) the mechanism of pop-out and recovery phenomenon at unloading. Note that in the enlarged views, the *van der Waals* interactions between the nanosheets are modeled by cohesive layers in FE (in blue, highlighted in a yellow background). (d) Stress propagation mechanism: (top) in terms of nanosheet delamination, the diagram depicts the effect of plane stress propagation on the P-h curve; (bottom) the plane stress spreading range with an increasing depth predicted by FE model using the equivalent conical indenter.

Figures 6a-b illustrate the origin of the distortions in the P-h curves owing to the slippage and delamination of the nanosheets, respectively. Regarding the slippage mode, initially, the indenter overcomes the interfacial forces that bind the nanosheets together (preventing separation of the nanosheets). The breakage of this interfacial constraint is indicated by the first broad hump in the schematic P-h curve (Figure 5b). Subsequently, the indenter starts to push apart the nanosheets sideward. The cohesive layers start to deform because of shear forces until complete failure occurs. More specifically, during the process, the increment of the resolved indention forces (P'_{nx}, $n = 1, 2, 3, \ldots$; where n stands for the numbering of the nanosheets) which are horizontally exerted between the indenter and the nanosheets decreases due to the growing detachment of the cohesive layers, and that is to say the interaction force between the adjacent nanosheets ($P_{\mathrm{interaction}}$) decreases gradually until the cohesive layer is fully damaged. This results in the pop-in segment of the P-h curve, corresponding to the slippage shown on the P-h curve (Figure 5b). By contrast the breakage of the cohesive layers progresses much slower in the delamination mode (than in the slippage mode, see Figure 6d) because the bending stress that induces delamination propagates slower than the acting shear stress while the nanosheets slide relative to one another. Therefore, the gradient of the distorted loading curve in delamination mode is reducing at a lower rate compared with the more abrupt stepwise pop-in deformation found in the slippage mode.

In the AFM nanoindentation experiments, we also observed the pop-out phenomenon during unloading. This suggests the formation of a new cohesive layer *via* the restoration of the broken *van der Waals* interactions between the nanosheets. The resolved counter-acting force from the indenter (P'_{nx}) is equivalent to the summation of the forces provided by the new cohesive layers ($P_{\mathrm{interaction}}$), the restraining forces exerted by the surrounding materials ($P_{\mathrm{surrounding}}$), and the friction force (P_{friction}). In fact, the friction also changes with the penetration of the indenter as a result of the varying normal force, and it can also affect the resultant P-h curves.[37] The model in Figure 6c shows that as the indenter continues to unload, the interaction force from the new cohesive layer increases, along with the declining force exerted by the surrounding material. Thus, resulting in a quasi-equilibrium state of the interplay between the indenter and the nanosheets, culminating in the pop-out deformation observed in the unloading curves. Interestingly, a force recovery process was witnessed in the experiment emerging right before the indenter-to-sample interaction was reduced to zero (Figure 5f). The reason of the recovery is like the pop-out phenomenon, but instead of reaching the force equilibrium, the augmentation of $P_{\mathrm{interaction}}$ was overwhelming compared with the reduction of $P_{\mathrm{surrounding}}$, therefore, the unloading P-h curve shows the rise in the resultant force (Figure 5d). We note that recovery appears when the unloading of the indenter is nearly completed, and at that moment $P_{\mathrm{surrounding}}$ is close to being fully relaxed. In the FE model, both the pop-out and recovery phenomena have been simulated.

Instead of indenting directly onto a thin stack of CuBDC nanosheets, on which the substrate effect on the elasticity measurement is prone to arise,[38] we performed the AFM nanoindentation experiments on the nanosheet stacks of at least 50 nm in thickness (~95 monolayers) to minimize the influence of substrate. Additionally, a few of the AFM nanoindentation experiments were performed on two thinner CuBDC nanosheet stacks (t ~ 16 nm and ~ 48 nm) placed on a glass substrate in order to investigate plasticity on the upper surface of the nanosheets. There were no visible radial cracks at the residual indents (Figures S4), which suggests the relatively resilient nature of the surrounding CuBDC framework. That is to say, the constraint imposed by the surrounding CuBDC framework has an impact (i.e. $P_{\mathrm{surrounding}}$) on the indentation area, and this is consistent with the force analysis in

Figure 6. In contrast, indentation experiments using a sharp indenter tip (e.g. cube-corner) on thin but stiffer layers such as the silicon (t ~ 50 nm),[39] and the hybrid YAS-GNP coating ($t = 169 \pm 10\ \mu$m) on a silicon carbide substrate[40] were reported to generate dramatic radial cracks.

Table 1. Threshold values of the indentation force, depth, projected area of indent, area of the stress field acquired based on Figure 6d (assuming it is a circular stress field propagating normal to the indentation direction), and stress (force/area of the stress field) leading to the three distinctive failure modes of a monolayer of the CuBDC nanosheet.

Threshold values / Failure modes	Force (nN)	Depth (Å)	Projected area of indent (nm^2)	Area of stress field (nm^2)	Stress (MPa)
Slippage	42.6	6.5	1.1	~ 2290	9.3
Fracture	70.4	6.4	1.1	~ 23779	3.0
Delamination	56.0	5.8	0.9	~ 3421	16.4

The P-h curves from AFM nanoindentation may show large-scale distortions as shown in Figure 5d. By characterizing such distortions, the threshold forces responsible for the failures of CuBDC nanosheets at the nanoscale can be quantified (Figure S12). We have estimated the threshold conditions triggering the failure modes I, II, and III of the CuBDC monolayer as summarized in Table 1; the evolution with indentation depth has also been characterized (Figure S13). Figure 6d shows that when the indentation depth is below ~2 nm, the stress spreading area of the slippage mode is less than the ones for delamination and fracture modes. However, when the indentation depth exceeds ~2 nm and ~2.5 nm, the stress area for slippage surpasses the areas for delamination and fracture, respectively. Likewise, we found that the threshold forces of the three modes in Table 1 are ranked in the same order. Accordingly, we found the stress required for delamination is ~1.8 times and ~5.5 times greater than the ones to induce slippage and fracture, respectively.

- **Small-scale continuous failures during AFM nanoindentation**

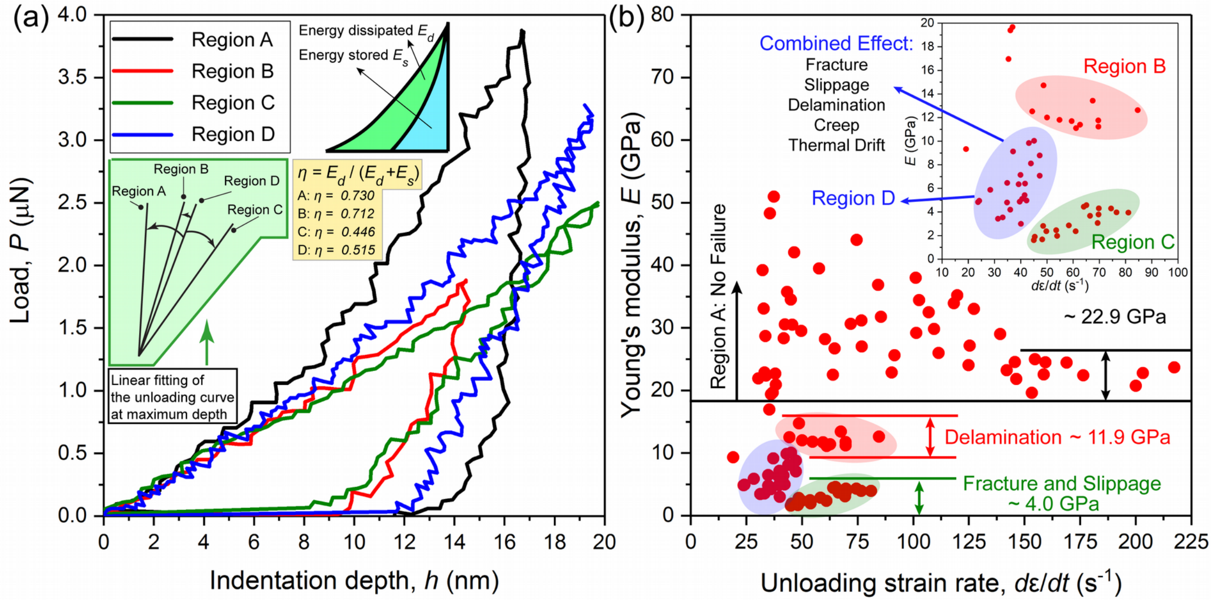

Figure 7. (a) Representative *P*-*h* curves from AFM nanoindentation of the CuBDC nanosheets showing indentations that cause: no failure (curve in black: region A), the delamination of nanosheets (curve in red: region B), coupled effect of the fracture and slippage of nanosheets (curve in green: region C), and a combination of all possible time-dependent responses such as creep, thermal drift, and the abovementioned failure modes (curve in blue: region D). Linear

fittings of the incipient unloading curves are shown in the green panel inset. Energy dissipation fraction (η) is given in the yellow panel inset. (b) Young's modulus determined using the Oliver and Pharr method from the unloading curves of the four types of P-h curves in (a), showing a significant loss of stiffness in regions B, C, and D versus region A.

In Figure 7a, the *P-h* curve in black obtained from AFM nanoindentation typifies the response of the CuBDC nanosheet without experiencing any kind of failure mode. While the other three representative *P-h* curves show distinct responses when indentation stress induces failure. Such a difference is exemplified in the scatter of the stiffness data in Figure 7b, indicating that the distribution of Young's moduli falls into four regions. Only region A describes the intrinsic property of CuBDC because of the absence of significant stress-induced framework failure and other time-dependent deformations (e.g. creep and thermal drift). Otherwise, the CuBDC framework could experience a varying degree of stiffness loss and reduced hardness (designated as regions B, C, and D) depending on the type of failure mode. Additionally, the energy loss (see Figure 7a) of the AFM nanoindentation experiments in regions B, C, and D was observed to be lower than in region A. The results suggest that in the scenarios described by region B, C, and D, part of the deformation was contributed by other forms of mechanical behaviors (e.g. fracture, sliding, and delamination) dissipating less energy relative to the plastic deformation in region A.

It is worth noting that the Young's moduli in regions B, C, and D of Figure 7b were derived from the *P-h* curves that exhibit no abrupt distortions over the history of the entire P-h curve. The data thus suggest that the occurrence of failures is a continuous process, compared to the characteristic failure modes evidenced in Figure 5d. The data points in region B might correspond to delamination of the CuBDC nanosheets (Mode III) induced by the AFM indenter.

This inference is based on the observation that delamination causes less additional indentation displacement than the other two failure modes, therefore, it brings about less stiffness loss. Conversely, indentation in region C may be attributed to the coupled effect of interfacial sliding (Mode I) and fracture (Mode II) of the nanosheets that results in a more considerable stiffness loss. The interfacial sliding in this study mainly refers to the horizontal sliding of nanosheets normal to the indenter axis, although the sliding along indentation direction may also cause stiffness loss, such as that reported by ref.41.

Regions B and C are the subsequently steady states of region D as the unloading strain rate increases. Akin to the effect of surpassing the time-dependent behaviors such as creep and thermal drift in the indention direction, sufficiently high unloading strain rate reduces the deformation of the nanosheets in the horizontal direction along $P'_{n\mathrm{x}}$, and thus contributing to the convergence of the Young's modulus from region D to C. With this in mind, the unloading strain rate principle[22] (see Methods) can also be extended to suppress the fracture mode since high loading-unloading strain rate shortens the time for cracks propagation. Figure 7b also shows that the indentations in region D were implemented at a relatively lower unloading strain rate, therefore the excessive additional indentation displacements were generated by a combination of factors: fracture, sliding, delamination, creep, and thermal drift. In this case, the unwanted effects of time-dependent processes can be suppressed by raising the unloading strain rate of the indenter.

IV. CONCLUSIONS

In this work, a quantitative approach is demonstrated for using the AFM-based nanoindentation technique to study the detailed mechanical properties of the CuBDC nanosheets. The main results are summarized as follows:

- Quantitative study of the nanoscale mechanics of 2-D nanosheets is challenging and this is especially true *via* AFM-based nanoindentation.

- The elastic-plastic properties including the Young's modulus and yield strength have been characterized. We demonstrate efficacy of the unloading strain rate principle for improving precision of the AFM nanoindentation measurements.

- Three characteristic failure modes at loading of the nanosheets have been proposed, namely the interfacial sliding (Mode I), framework fracture (Mode II), and delamination (Mode III). The mechanisms are controlled by the interlayer shear deformation, framework rupture, and bending deformation, respectively. The threshold indentation forces and threshold indentation depths of each of the failure modes have been established.

- Finite-element modeling (FEM) has been employed to simulate the AFM nanoindentation of the MOF nanosheets to gain insights into the deformation mechanisms underpinning plasticity and failure modes. The model also explains the pop-out and recovery phenomena observed in the nanosheets during nanoindenter unloading.

- Although the CuBDC nanosheets were chosen in this study as a model material to develop the AFM nanoindentation of metal-organic nanosheets, the general methodologies described are transferrable to probe a wide range of 2-D *van der Waals* layered systems.

METHODS

Synthesis and Characterization of CuBDC Nanosheets

The CuBDC nanosheets were synthesized using the layering technique reported by Rodenas *et al*.[10] The synthesis steps are described in section 1 of the Supporting Information (SI). The morphology of the nanosheets was examined using the Carl Zeiss Evo LS15 VP scanning electron microscope (Figure 2a), the JEM-2100 LaB6 transmission electron microscope (Figure 2b), and the Veeco Dimension 3100 atomic force microscope equipped with the Tap300Al-G probe in tapping mode (Figure 2c). The crystal structure of the CuBDC nanosheets was confirmed by powder X-ray diffraction (XRD) using the Rigaku Miniflex diffractometer (Figure 2d).

AFM Nanoindentation using a Diamond-Tipped Cantilever Probe

AFM nanoindentation measurements were performed using the Veeco Dimension 3100 instrument operating under the indentation mode, equipped with the Bruker PDNISP probe (a cube-corner diamond tip, see SI Figure S1). The probe has a 350-μm long cantilever made of stainless steel, where a cube-corner diamond indenter tip is mounted at the end of the cantilever. The spring constant and contact sensitivity of the probe have been calibrated, and given as 152.285 N/m and 256.6 nm/volt, respectively.

AFM Nanoindentation Methodology and Analysis of P-h Data

Oliver and Pharr Method

Each AFM nanoindentation experiment generates a force-displacement (P-h) curve, which was analyzed using the Oliver and Pharr (OP) method to determine the Young's modulus

(E) of the CuBDC nanosheets.[42] Every data point of E in Figure 3b was obtained from an individual indentation cycle, comprising a single loading-unloading cycle.

Unloading Strain Rate Method

Indentation on materials that are either porous or brittle and either viscoelastic or defective, usually exhibits failures or creep, which can introduce significant distortions on the P-h curves and under these circumstances, the OP method is no longer suitable. It was found that at the unloading stage, the additional displacement along the indentation direction still dominate the overall movement overwhelming the elastic recovery towards the opposite (*viz.* unloading) direction.[22] Consequently, the incipient segment of the unloading curve no longer reflects the ability of the specimen to resist deformation in response to the applied indentation load. To overcome this limitation, an augmented unloading strain rate method[22] was implemented to retrieve the P-h curves that better reflect the true elastic-plastic response of the nanosheets. In fact, for the nanosheets, the in-plane stretch may also affect the measurement of stiffness.[43]

Iterative Method for Determining Plasticity

In the FE model, the elastic-plastic material properties were defined as listed in Table S3. For elasticity, the Young's modulus can be measured using AFM nanoindentation (Figure 3). For plasticity, at first, it was assumed that the strength coefficient (k) of CuBDC is relatively high ($\gtrsim$150), meanwhile, the work-hardening exponent (n) is in the range of 0.1 to 0.3 (these assumptions were later verified since $n \sim 0.17275$ and $k \sim 863.52053$ were obtained using the iterative method). And in this case, the plastic behavior of material was assumed to follow a power-law relation using the Hollomon's equation.[44] The work-hardening exponent n exerts an influence on the height of the pile-ups by inhibiting the formation of pile-ups.[42] In detail, the hardening of the material near the indenter actually restrains the rising flow towards the surface of the sample. For this reason, the work-hardening property of the CuBDC nanosheets was considered, this can be associated with the collapse of MOF nanopores leading to densification of the open framework. The relation between the stress (σ) and plastic strain (ε_p) in the Hollomon's equation is given by:[45]

$$\sigma = k \cdot \varepsilon_p^{\ n} \tag{1}$$

Since at the end of the elastic regime of a stress-strain curve, the strength coefficient (k) can also be defined based on the elastic modulus:

$$k = \frac{\sigma_y}{(\varepsilon)^n} = \frac{\sigma_y}{\left(\frac{\sigma_y}{E}\right)^n} \tag{2}$$

In addition, according to the empirical relation proposed by Matthews, the ratio between the height of residual pile-up, s, after the withdrawal of the indenter tip and the indentation depth at the maximum load, h (see Figure 4c), was assigned based on the work-hardening exponent (n):[46]

$$\frac{s}{h} = \frac{1}{2}\left(\frac{2+n}{2}\right)^{2(1-n)/n} - 1 \tag{3}$$

The value of s can be measured from the AFM images of the indents (Figure 4a-c). The study of 32 indents gave the arithmetic mean value of $s/h \sim 0.10551$ (SI, Table S2), and thus $n = 0.17275$.

In the iterative procedure, an initial estimated value of the yield stress (σ_y) was assigned to equation (2) acquiring an initial value of k. Subsequently, by substituting the values of k and n into equation (1), this gives the first predicted plasticity property of the CuBDC nanosheets.

Inputting the elastic modulus ($E \sim 22.9$ GPa) and the predicted plastic property into the FE model, gives a new value of s/h. Through the iterative process, we found the values of σ_y ~448.8 MPa (Figure 4g) and k ~863.52053; the convergence criterion is met when the FE model with an updated input value of σ_y returns the s/h ratio that matches the one measured from AFM nanoindentation, *viz.* $s/h \sim 0.10551$.

Finite-Element (FE) Modeling

For the purpose of predicting the plastic deformation of the CuBDC nanosheets (Figure 4), we use the finite-element method (FEM) as implemented in the ABAQUS CAE program to simulate the indenter-to-sample contact and non-linear structural deformations. The continuum slab model representing the CuBDC nanosheets was meshed using the 8-node linear brick elements with reduced integration and hourglass control (*C3D8R*). We employed the ABAQUS/Explicit solver[47] which is tailored for calculating complex contact mechanics problems. It is noted that the oscillations of P-h curves reported in the literature[48,49] have been overcome by applying a refined mesh in this study. The indenter in the FE model is a discrete rigid cone with equivalent inclusive angle as the real indenter, in which a curved apex with a radius of $r = 22.1$ nm was created to prevent excessive mesh distortion.

FEM with the ABAQUS/Explicit solver has also been employed to model the patterns of distortions (Figure 5) caused by the failures of the CuBDC nanosheets during the loading stage as well as the recovery and pop-out phenomena during unloading. In these FE models where the nanosheet interfacial failures were defined, the interaction between the adjacent nanosheets was modelled using the cohesive elements whose damage under stress initiates based on the maximum nominal stress criterion (SI section 6). Moreover, we apply the Johnson-Cook fracture criterion to model the fracture of the nanosheets under the penetration of the indenter, allowing the strain rate effects to be studied (SI section 7).[50] The Johnson-Cook model was initially proposed for metals, but has also been applied to softer materials like polymers.[51]

ASSOCIATED CONTENT

Supporting Information

Synthesis method, characterization of the geometry of the cube-corner indenter tip, AFM topology of the nanosheets and the residual indents, the ratio of the pile-up height to the indentation depth, the iterative method for determining plasticity, finite element models, the influence of the varying Poisson's ratios on the quantification of the Young's modulus, as well as the threshold forces and depths resulting in the different failure modes.

AUTHOR INFORMATION

Corresponding Author

*E-mail: jin-chong.tan@eng.ox.ac.uk

ORCID

Jin-Chong Tan: 0000-0002-5770-408X

Zhixin Zeng: 0000-0002-7871-3970

Author Contributions

Z.X.Z. performed the AFM nanoindentation experiments and FEM simulations. I.S.F. synthesized the nanosheet samples and performed the SEM and TEM imaging. Z.X.Z. analyzed the data and prepared the figures under the supervision of J.C.T. Z.X.Z. and J.C.T. wrote the manuscript with input from all authors.

Notes

The authors declare no competing financial interest.

ACKNOWLEDGEMENTS

This work was supported by the ERC Consolidator Grant through the grant agreement 771575 (PROMOFS). The authors acknowledge the Research Complex at Harwell (RCaH) for access to the materials characterization facilities. I.S.F. thanks Dr James Gilchrist for the training and assistance in collecting the TEM images. We are grateful to Dr Gavin Stenning and Dr Marek Jura at R53 Materials Characterization Laboratory (ISIS Rutherford Appleton Laboratory) for providing access to the XRD facilities.

REFERENCES

1. Tan, J. C.; Cheetham, A. K., Mechanical properties of hybrid inorganic–organic framework materials: establishing fundamental structure–property relationships. *Chem. Soc. Rev.* **2011,** *40*, 1059-1080.

2. Allendorf, M. D.; Stavila, V., Crystal engineering, structure–function relationships, and the future of metal–organic frameworks. *CrystEngComm* **2015,** *17*, 229-246.

3. Howarth, A. J.; Liu, Y.; Li, P.; Li, Z.; Wang, T. C.; Hupp, J. T.; Farha, O. K., Chemical, thermal and mechanical stabilities of metal–organic frameworks. *Nat. Rev. Mater.* **2016,** *1*, 15018.

4. Cavallo, F.; Grierson, D. S.; Turner, K. T.; Lagally, M. G., "Soft Si": Effective Stiffness of Supported Crystalline Nanomembranes. *ACS Nano* **2011,** *5*, 5400-5407.

5. Jiang, Z.; Li, Z.; Qin, Z.; Sun, H.; Jiao, X.; Chen, D., LDH nanocages synthesized with MOF templates and their high performance as supercapacitors. *Nanoscale* **2013,** *5*, 11770-11775.

6. Cao, F.; Zhao, M.; Yu, Y.; Chen, B.; Huang, Y.; Yang, J.; Cao, X.; Lu, Q.; Zhang, X.; Zhang, Z.; Tan, C.; Zhang, H., Synthesis of Two-Dimensional CoS1.097/Nitrogen-Doped Carbon Nanocomposites Using Metal–Organic Framework Nanosheets as Precursors for Supercapacitor Application. *J. Am. Chem. Soc.* **2016,** *138*, 6924-6927.

7. Chhowalla, M.; Shin, H. S.; Eda, G.; Li, L. J.; Loh, K. P.; Zhang, H., The chemistry of two-dimensional layered transition metal dichalcogenide nanosheets. *Nat. Chem.* **2013,** *5*, 263.

8. Zhao, S.; Wang, Y.; Dong, J.; He, C. T.; Yin, H.; An, P.; Zhao, K.; Zhang, X.; Gao, C.; Zhang, L.; Lv, J.; Wang, J.; Zhang, J.; Khattak, A. M.; Khan, N. A.; Wei, Z.; Zhang, J.; Liu, S.; Zhao, H.; Tang, Z., Ultrathin metal–organic framework nanosheets for electrocatalytic oxygen evolution. *Nat. Energy.* **2016,** *1*, 16184.

9. Chaudhari, A. K.; Kim, H. J.; Han, I.; Tan, J. C., Optochemically Responsive 2D Nanosheets of a 3D Metal–Organic Framework Material. *Adv. Mater.* **2017,** *29*, 1701463.

10. Rodenas, T.; Luz, I.; Prieto, G.; Seoane, B.; Miro, H.; Corma, A.; Kapteijn, F.; Llabrés i Xamena, F. X.; Gascon, J., Metal–organic framework nanosheets in polymer composite materials for gas separation. *Nat. Mater.* **2015,** *14*, 48.

11. Zhou, W.; Wu, H.; Yildirim, T., Structural stability and elastic properties of prototypical covalent organic frameworks. *Chem. Phys. Lett.* **2010,** *499*, 103-107.

12. Hosseini, E.; Zakertabrizi, M.; Habibnejad Korayem, A.; Chang, Z., Mechanical and electromechanical properties of functionalized hexagonal boron nitride nanosheet: A density functional theory study. *J. Chem. Phys.* **2018,** *149*, 114701.

13. Eshkalak, K. E.; Sadeghzadeh, S.; Jalaly, M., Mechanical properties of defective hybrid graphene-boron nitride nanosheets: A molecular dynamics study. *Comput. Mater. Sci.* **2018,** *149*, 170-181.

14. Abadi, R.; Uma, R. P.; Izadifar, M.; Rabczuk, T., Investigation of crack propagation and existing notch on the mechanical response of polycrystalline hexagonal boron-nitride nanosheets. *Comput. Mater. Sci.* **2017,** *131*, 86-99.

15. Mortazavi, B.; Cuniberti, G., Mechanical properties of polycrystalline boron-nitride nanosheets. *RSC Adv.* **2014,** *4*, 19137-19143.

16. Ansari, R.; Rouhi, S.; Ajori, S., Elastic properties and large deformation of two-dimensional silicene nanosheets using molecular dynamics. *Superlattices Microstruct.* **2014,** *65*, 64-70.

17. Falin, A.; Cai, Q.; Santos, E. J. G.; Scullion, D.; Qian, D.; Zhang, R.; Yang, Z.; Huang, S.; Watanabe, K.; Taniguchi, T.; Barnett, M. R.; Chen, Y.; Ruoff, R. S.; Li, L. H., Mechanical properties of atomically thin boron nitride and the role of interlayer interactions. *Nat. Commun.* **2017,** *8*, 15815.

18. Penkov, O. V.; Pukha, V. E.; Devizenko, A. Y.; Kim, H. J.; Kim, D. E., Self-Healing Phenomenon and Dynamic Hardness of C60-Based Nanocomposite Coatings. *Nano Lett.* **2014,** *14*, 2536-2540.

19. Ozden, S.; Yang, Y.; Tiwary, C. S.; Bhowmick, S.; Asif, S.; Penev, E. S.; Yakobson, B. I.; Ajayan, P. M., Indentation Tests Reveal Geometry-Regulated Stiffening of Nanotube Junctions. *Nano Lett.* **2016,** *16*, 232-236.

20. Lee, C.; Wei, X.; Kysar, J. W.; Hone, J., Measurement of the Elastic Properties and Intrinsic Strength of Monolayer Graphene. *Science* **2008,** *321*, 385-388.

21. Payamyar, P.; Kaja, K.; Ruiz-Vargas, C.; Stemmer, A.; Murray, D. J.; Johnson, C. J.; King, B. T.; Schiffmann, F.; VandeVondele, J.; Renn, A.; Götzinger, S.; Ceroni, P.; Schütz, A.; Lee, L. T.; Zheng, Z.; Sakamoto, J.; Schlüter, A. D., Synthesis of a Covalent Monolayer Sheet by Photochemical Anthracene Dimerization at the Air/Water Interface and its Mechanical Characterization by AFM Indentation. *Adv. Mater.* **2014,** *26*, 2052-2058.

22. Zeng, Z.; Tan, J. C., AFM Nanoindentation To Quantify Mechanical Properties of Nano- and Micron-Sized Crystals of a Metal–Organic Framework Material. *ACS Appl. Mater. Interfaces* **2017,** *9*, 39839-39854.

23. Lin, Q. Y.; Zeng, Y. H.; Liu, D.; Jing, G. Y.; Liao, Z. M.; Yu, D., Step-by-Step Fracture of Two-Layer Stacked Graphene Membranes. *ACS Nano* **2014,** *8*, 10246-10251.

24. Huang, P.; Guo, D.; Xie, G.; Li, J., Softened Mechanical Properties of Graphene Induced by Electric Field. *Nano Lett.* **2017,** *17*, 6280-6286.

25. Xu, J.; Yuan, G.; Zhu, Q.; Wang, J.; Tang, S.; Gao, L., Enhancing the Strength of Graphene by a Denser Grain Boundary. *ACS Nano* **2018,** *12*, 4529-4535.

26. Kim, S. M.; Hsu, A.; Park, M. H.; Chae, S. H.; Yun, S. J.; Lee, J. S.; Cho, D. H.; Fang, W.; Lee, C.; Palacios, T.; Dresselhaus, M.; Kim, K. K.; Lee, Y. H.; Kong, J., Synthesis of large-area multilayer hexagonal boron nitride for high material performance. *Nat. Commun.* **2015,** *6*, 8662.

27. Kong, D.; Megone, W.; Nguyen, K. D. Q.; Di Cio, S.; Ramstedt, M.; Gautrot, J. E., Protein Nanosheet Mechanics Controls Cell Adhesion and Expansion on Low-Viscosity Liquids. *Nano Lett.* **2018,** *18*, 1946-1951.

28. Tan, J. C.; Saines, P. J.; Bithell, E. G.; Cheetham, A. K., Hybrid Nanosheets of an Inorganic–Organic Framework Material: Facile Synthesis, Structure, and Elastic Properties. *ACS Nano* **2012,** *6*, 615-621.

29. Guo, L.; Yan, H.; Moore, Q.; Buettner, M.; Song, J.; Li, L.; Araujo, P. T.; Wang, H. T., Elastic properties of van der Waals epitaxy grown bismuth telluride 2D nanosheets. *Nanoscale* **2015,** *7*, 11915-11921.

30. Hermosa, C.; Horrocks, B. R.; Martínez, J. I.; Liscio, F.; Gómez-Herrero, J.; Zamora, F., Mechanical and optical properties of ultralarge flakes of a metal–organic framework with molecular thickness. *Chem. Sci.* **2015,** *6*, 2553-2558.

31. Jariwala, D.; Marks, T. J.; Hersam, M. C., Mixed-dimensional van der Waals heterostructures. *Nat Mater* **2016**.

32. Mori, W.; Inoue, F.; Yoshida, K.; Nakayama, H.; Takamizawa, S.; Kishita, M., Synthesis of New Adsorbent Copper(II) Terephthalate. *Chem. Lett.* **1997,** *26*, 1219-1220.

33. Coleman, J. N.; Lotya, M.; O'Neill, A.; Bergin, S. D.; King, P. J.; Khan, U.; Young, K.; Gaucher, A.; De, S.; Smith, R. J.; Shvets, I. V.; Arora, S. K.; Stanton, G.; Kim, H. Y.; Lee, K.; Kim, G. T.; Duesberg, G. S.; Hallam, T.; Boland, J. J.; Wang, J. J.; Donegan, J. F.; Grunlan, J. C.; Moriarty, G.; Shmeliov, A.; Nicholls, R. J.; Perkins, J. M.; Grieveson, E. M.; Theuwissen, K.; McComb, D. W.; Nellist, P. D.; Nicolosi, V., Two-Dimensional Nanosheets Produced by Liquid Exfoliation of Layered Materials. *Science* **2011,** *331*, 568-571.

34. Carson, C. G.; Hardcastle, K.; Schwartz, J.; Liu, X.; Hoffmann, C.; Gerhardt, R. A.; Tannenbaum, R., Synthesis and Structure Characterization of Copper Terephthalate Metal–Organic Frameworks. *Eur. J. Inorg. Chem.* **2009,** *2009*, 2338-2343.

35. Taljat, B.; Pharr, G. M., Development of pile-up during spherical indentation of elastic–plastic solids. *Int J Solids Struct.* **2004,** *41*, 3891-3904.

36. Loganathan, A.; Sharma, A.; Rudolf, C.; Zhang, C.; Nautiyal, P.; Suwas, S.; Boesl, B.; Agarwal, A., In-situ deformation mechanism and orientation effects in sintered 2D boron nitride nanosheets. *Mater. Sci. Eng. A* **2017,** *708*, 440-450.

37. Bédoui, F.; Sansoz, F.; Murthy, N. S., Incidence of nanoscale heterogeneity on the nanoindentation of a semicrystalline polymer: Experiments and modeling. *Acta Mater.* **2008,** *56*, 2296-2306.

38. Fisher-Cripps, A. C., *Nanoindentation*. 2nd ed.; Springer, New York: 2004.

39. Pharr, G. M.; Oliver, W. C.; Harding, D. S., New evidence for a pressure-induced phase transformation during the indentation of silicon. *J. Mater. Res.* **1991,** *6*, 1129-1130.

40. Garcia, E.; Nistal, A.; Khalifa, A.; Essa, Y.; Martín de la Escalera, F.; Osendi, M. I.; Miranzo, P., Highly Electrically Conducting Glass-Graphene Nanoplatelets Hybrid Coatings. *ACS Appl. Mater. Interfaces* **2015,** *7*, 17656-17662.

41. Chen, Y.; Bakshi, S. R.; Agarwal, A., Intersplat Friction Force and Splat Sliding in a Plasma-Sprayed Aluminum Alloy Coating during Nanoindentation and Microindentation. *ACS Appl. Mater. Interfaces* **2009,** *1*, 235-238.

42. Oliver, W. C.; Pharr, G. M., Measurement of hardness and elastic modulus by instrumented indentation: Advances in understanding and refinements to methodology. *J. Mater. Res.* **2004,** *19*, 3-20.

43. Costa, K. D.; Yin, F. C., Analysis of indentation: implications for measuring mechanical properties with atomic force microscopy. *J. Biomech. Eng.* **1999,** *121*, 462-71.

44. Bowen, A. W.; Partridge, P. G., Limitations of the Hollomon strain-hardening equation. *J. Phys. D Appl. Phys.* **1974,** *7*, 969-978.

45. Hollomon, J. H., Tensile Deformation. *Trans. Metall. Soc. AIME* **1945,** *162*, 268-290.

46. Matthews, J. R., Indentation hardness and hot pressing. *Acta Metall.* **1980,** *28*, 311-318.

47. Hibbitt, K. S., Inc., ABAQUS Analysis User's Guide. **2016**.

48. Bocciarelli, M.; Bolzon, G.; Maier, G., Parameter identification in anisotropic elastoplasticity by indentation and imprint mapping. *Mech. Mater.* **2005,** *37*, 855-868.

49. Chen, Z.; Wang, X.; Atkinson, A.; Brandon, N., Spherical indentation of porous ceramics: Elasticity and hardness. *J. Eur. Ceram. Soc.* **2016,** *36*, 1435-1445.

50. Johnson, G. R.; Cook, W. H., Fracture characteristics of three metals subjected to various strains, strain rates, temperatures and pressures. *Eng. Fract. Mech.* **1985,** *21*, 31-48.

51. Louche, H.; Piette-Coudol, F.; Arrieux, R.; Issartel, J., An experimental and modeling study of the thermomechanical behavior of an ABS polymer structural component during an impact test. *Int. J. Impact. Eng.* **2009,** *36*, 847-861.